Title

The Millikan shaking experiments and high-frequency seismic wave propagation in Southern California

Journal

Geophysical Journal International, 198(2)

ISSN

0956-540X

Authors

Tanimoto, Toshiro
Okamoto, Taro

Publication Date

2014-08-01

DOI

10.1093/gji/ggu189

Peer reviewed

Geophysical Journal International

Geophys. J. Int. (2014) **198,** 1081–1095 doi: 10.1093/gji/ggu189
GJI Seismology

The Millikan shaking experiments and high-frequency seismic wave propagation in Southern California

Toshiro Tanimoto[1] and Taro Okamoto[2]

[1]*Department of Earth Science, University of California, Santa Barbara, CA 93106, USA. E-mail: toshiro@geol.ucsb.edu*
[2]*Department of Earth and Planetary Sciences, Tokyo Institute of Technology, Meguro-ku, Tokyo, Japan*

Accepted 2014 May 20. Received 2014 May 19; in original form 2014 February 3

SUMMARY

In order to study high-frequency seismic wave propagation, seismic wavefields generated by resonant-shaking experiments of the Millikan Library, on the campus of California Institute Technology (Pasadena, California, USA), were analysed. Because the resonant shaking frequencies are 1.12 Hz (the east–west direction) and 1.64 Hz (the north–south direction), this active-source experiment can provide opportunities for studying high-frequency seismic wave propagation in Southern California. Because they are very narrow frequency band data, the analyses must be quite different from ordinary time-domain analyses. We show, theoretically, that the signals must be dominated by surface waves. Adopting this surface wave assumption, we proceed to make two separate analyses, one on spectral amplitude and the other on phase. We present a new method to derive group velocity from phase based on the cross correlations between the station in the Millikan Library (MIK) and stations in the regional network. Our results support that an active-source experiment by resonant shaking of a building is a feasible approach for high-frequency seismic wave studies.

Key words: Controlled source seismology; Body waves; Surface waves and free oscillations; Wave propagation.

1 INTRODUCTION

One of the challenges for seismologists is to improve our ability to predict high-frequency earthquake ground motions, especially above 1 Hz, at the time of major earthquakes. This is important because many buildings have resonant frequencies above 1 Hz, but we are still incapable of modelling such high-frequency waves.

This challenge is difficult because of two reasons; first, we lack understanding on how high-frequency waves are excited on earthquake faults. It is puzzling how some earthquakes generated accelerations that were more than $1 \times g$, that is, gravitational acceleration ($\approx$9.8 m s^{-2}). One extreme example, the 2008 Minami–Iwate earthquake in Northern Japan, showed the maximum acceleration of $3.8 \times g$, which is difficult to understand to say the least. The second reason is that we lack a suitable earth model that can explain high-frequency seismic wave propagation, including codas of major phases. This is clearly a problem of small-scale heterogeneity, which has not been built into most earth models so far. These two aspects of problems are quite hard and undoubtedly require sustained efforts by seismologists for sometime to come.

This paper is an attempt to make progress for the second problem on wave propagation. We seek a new way to understand high-frequency wave propagation and improve our knowledge of the crustal structure. We approach this question by an active-source experiment. But instead of a typical active source like an explosion or a vibroseis instrument, our excitation source is the Millikan library on the campus of California Institute of Technology in Pasadena, California, USA. We analyse seismic wavefields that were generated by shaking this building at its resonant frequencies, and were recorded by the regional broad-band seismograph network (California Integrated Seismograph Network, hereafter CISN).

Our approach is a modest attempt in terms of the frequency range; because good signals can only propagate at the resonant frequencies of the Millikan library, our analysis is limited to 1.12 and 1.64 Hz. But the results seem to indicate that a deterministic modelling, such as those performed for a lower frequency range ($<$0.5 Hz), may still work at these frequencies as we can measure group velocities for many paths. Scattering effects must be incorporated as phase scatter becomes larger but the phase coherence between stations, even at distances beyond 100 km, can be confirmed for many station pairs.

This paper proceeds in the following way; we give a brief introduction on the geography and the Millikan library experiments in Section 2. In Section 3, we present records from CISN, specifically focusing on amplitude–distance relationship. In Section 4, we present our theoretical and numerical analysis of the nature of waves in signals. Based on this, we present a simple constraint on the parameter QU in Section 5, where Q is attenuation and U is group velocity of surface waves. In Section 6, we discuss our results on phase data which will be derived by deconvolving source effects by using seismic records at MIK, a station in the Millikan library. We are able to determine group velocity of Rayleigh waves for 25 station pairs. Summary of conclusions is given in Section 7.

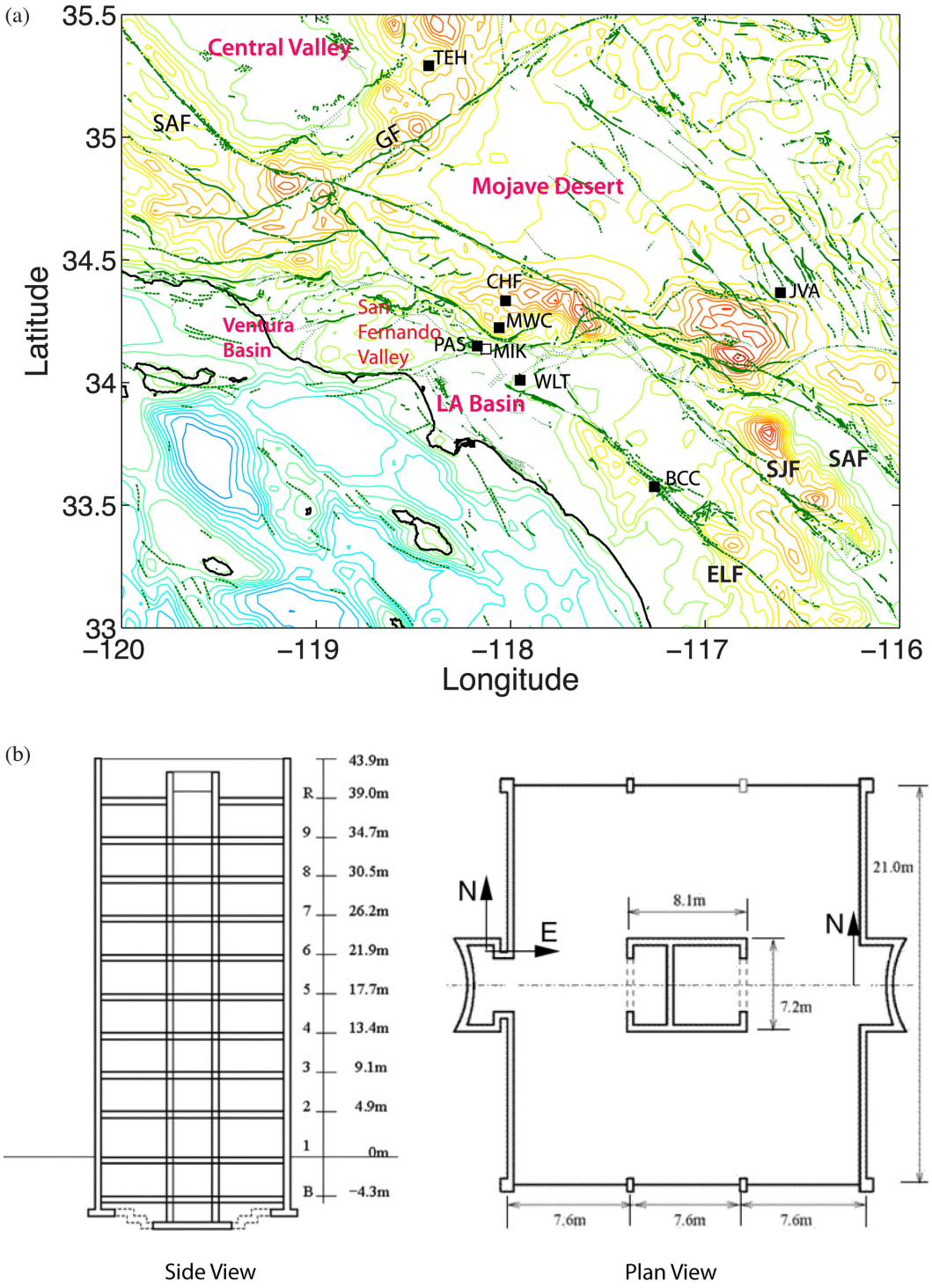

Figure 1. (a) The location of the Millikan library is denoted by an open square which is also the location of seismic station MIK. Locations of selected stations from the regional network, PAS, MWC, CHF, WLT, JVA, BCC and TEH, are shown whose waveforms or spectra (amplitude and phase) are discussed later. Major faults are denoted as SAF (San Andreas fault), SJF (San Jacinto fault), ELF (Elsinore fault) and GF (Garlock fault). Boundary of the Los Angeles basin can be recognized in a later figure (Fig. 7) as the boundary of green area in that figure. (b) An approximate dimension of the Millikan library. Its height is 43 m, the north–south extent 21 m and the east–west extent is 22.8 m. This information is from Bradford *et al.* (2004), Favela (2004) and Clinton *et al.* (2006) which contain more detailed information.

2 BACKGROUND

Fig. 1(a) shows a fault map of Southern California. Most faults in the region are drawn by green lines with some major ones denoted as SAF (the San Andreas fault), GF (the Garlock fault), SJF (the San Jacinto Fault) and ELF (the Elsinore fault). The Millikan library is denoted by an open square near the centre which also houses a seismic station MIK. This is on the campus of California Institute of Technology and is located near the northern edge of the Los

Angeles Basin. An approximate area of the Los Angeles basin can be seen in a later figure (Fig. 7) as a large green area and is the major metropolitan area of Los Angeles. Selected stations (PAS, MWC, WLT, BCC, JVA and TEH) from the regional broad-band seismic network are shown in this figure whose waveforms and spectra are discussed in later sections.

Scale of the Millikan library is shown in Fig. 1(b); The left panel shows that its height is 43.9 m with the basement reaching 4.3 m into the ground. The plan view on the right shows that its north–south extent is 21 m and its east–west extent is 22.8 m. More details can be found in Bradford *et al.* (2004), Favela (2004) and Clinton *et al.* (2006).

The Millikan-library shaking experiments have a long history since the late 1960s when the building was still under construction (Kuroiwa & Jennings 1968; Kuroiwa 1969). Its characteristics, especially its resonance frequencies, have been studied repeatedly over the last 40 yr. The results were reported in Kuroiwa (1969), Foutch (1976), Foutch & Jennings (1978), Clinton (2004), Bradford *et al.* (2004) and Clinton *et al.* (2006). The last three papers present a good summary of previous experiments up to their publication. With the recent installation of seismographs on every floor, the characteristics of the building were analysed again by modern interferometry approaches by Snieder & Safak (2006), Kohler *et al.* (2007) and Newton & Snieder (2012).

The target of these studies were to understand the vibration characteristics of the building itself and were not on the wavefields generated by shaking experiments. Despite the fact that the first report of teleseismic signal detection was early (Jennings 1970), the idea of using it as an active source of seismic waves has not been seriously pursued until recently (e.g. Favela 2004). This may be partly due to the fact that a dense broad-band network with digital recordings was not available in the region until about 15 yr ago. But since the late 1990s, there is a dense digital broad-band network in Southern California and we can take advantage of it by performing the Millikan shaking experiments.

3 DATA

The results of this paper are based on four experiments. Two of them were conducted on 2001 August 3 and 2002 September 23 and were the north–south shaking experiments. The predominant frequency was 1.64 Hz. The other two experiments were conducted on 2002 February 19, and 2002 September 19 and were the east–west shaking experiments. The predominant frequency for these experiments were 1.12 Hz.

Below we use a subset of data to illustrate the characteristics of shaking experiments but in the final results for amplitude, we will include all results from four experiments. For phase analysis in later sections, we analysed only the 1.64 Hz data as the quality and quantity of data were somehow low for the 1.12 Hz (east–west shaking) data.

3.1 Amplitudes in the excited wavefield

Fig. 2(a) shows a time–frequency plot of seismogram at PAS (Pasadena) for the entire day on 2001 August 3. A 4-hr-long, north–south shaking experiment was conducted on this day. The station PAS is about 4.36 km to the west of the Millikan library. The ordinate is frequency (Hz) and the abscissa is time (hour, UTC). Fourier spectral amplitudes in velocity are plotted by using three colours; blue is low amplitude, yellow is intermediate and red is high amplitude. Unit for amplitude is metres per second because we normalize spectra by the length of time-series.

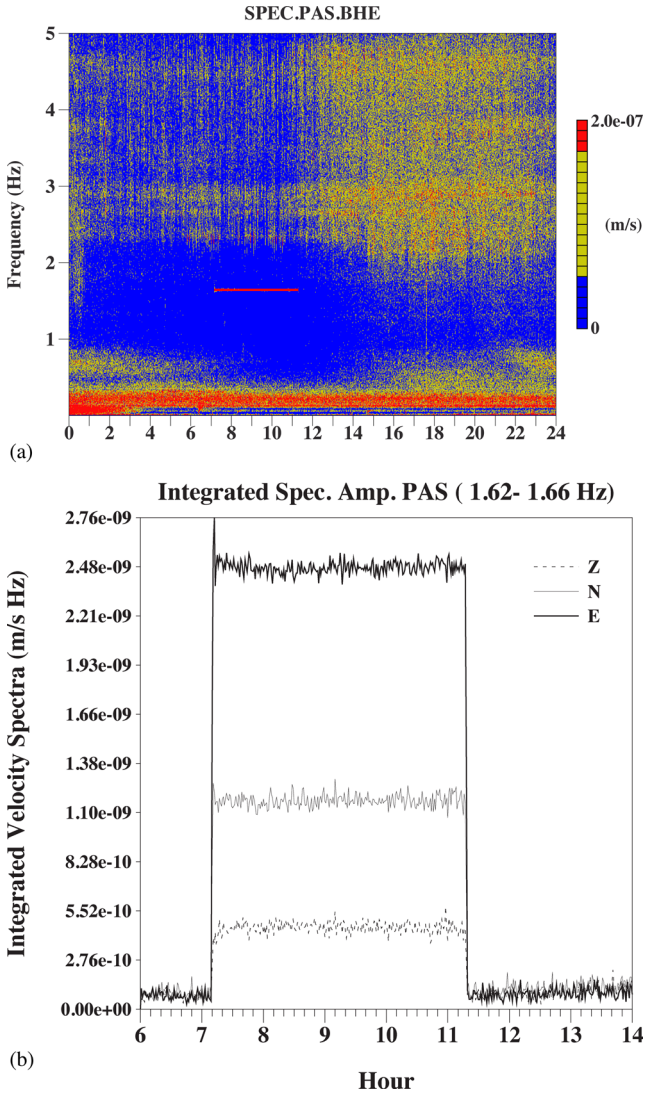

Figure 2. (a) Time–frequency plot of data at PAS on 2001 August 3. The north–south shaking experiment was conducted approximately from the hour 7 to hour 11 (red line at 1.64 Hz). Spectral amplitudes in unit of metres per second (normalized by the length of time-series) are shown. Three colours indicate low amplitude (blue), intermediate amplitude (yellow) and high amplitude (red). Red region below 0.3 Hz was generated by microseisms. Generally lower amplitudes on the left-half between 2 and 5 Hz and high amplitudes on the right-half are the contrast between night and day. Time is UTC. (b) The integrated spectral amplitudes from 1.62 Hz to 1.66 Hz for the experiment on 2001 August 3 (Fig. 1a). Except for the initial overshoot of amplitude, the excitation was maintained at about the same amplitude. This was also the case for three other experiments.

Fig. 2(a) shows general features of the background seismic noise in addition to the signal from the Millikan library; the first is the high-amplitude microseism noise that is clear below about 0.3 Hz (red). A high-amplitude noise persists for the whole 24 hr period. The other is reflected in the patterns between about 2 and 5 Hz, where yellow and red regions increase from left to right. Stronger yellow (with red) on the right-half of this plot indicates that the daytime cultural noise higher than the night-time noise in Pasadena.

We focus on the signals from the Millikan library that showed up as the red line at 1.64 Hz from about the hour 7 to the hour 11.

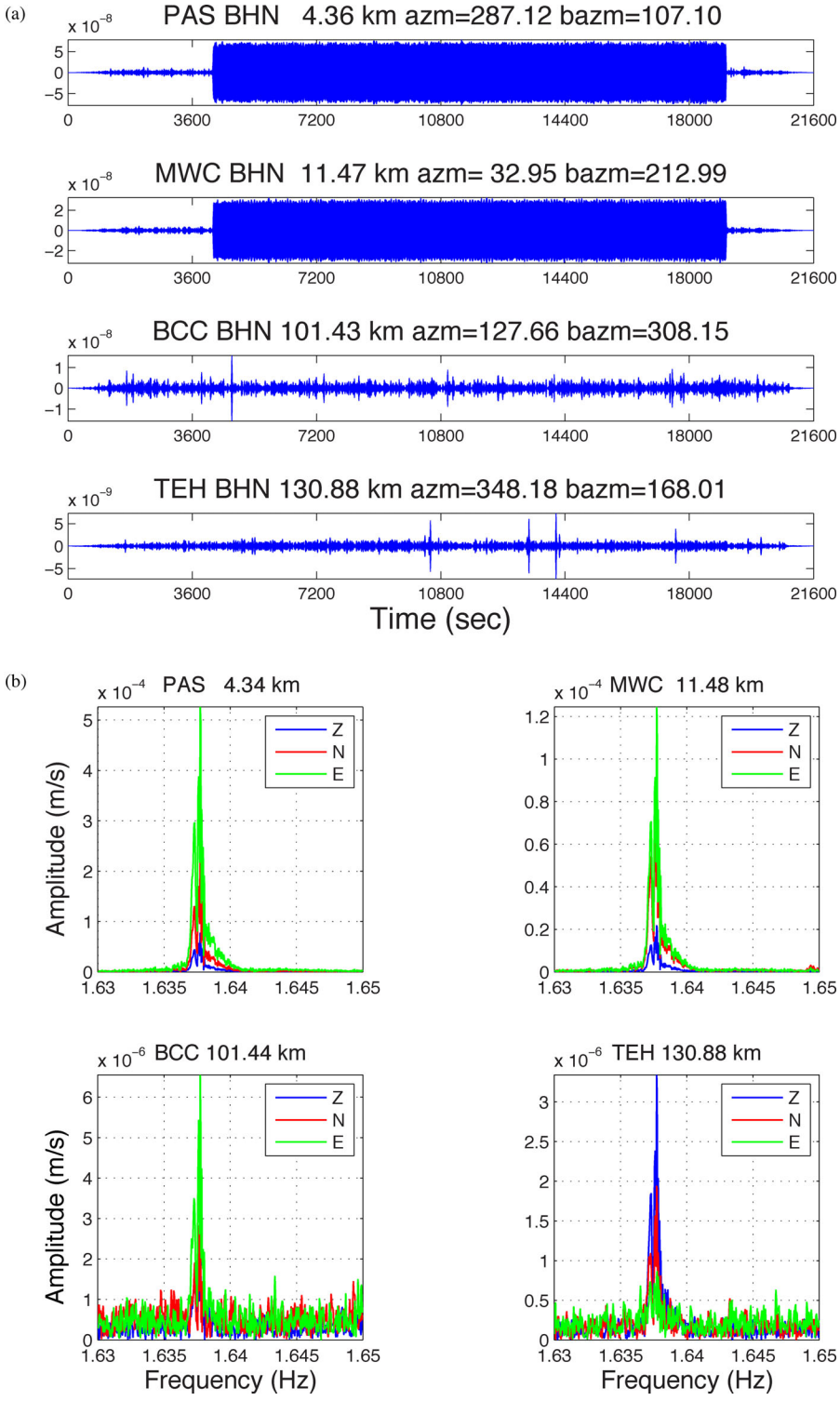

Figure 3. (a) Time-domain waveforms for the experiment on 2001 August 3. Envelopes in the time domain are like box-cars at nearby stations (PAS and MWC) but they disappear at distance stations (BCC and TEH). (b) Fourier spectra for four stations in Fig. 3(a). They were computed by using the time-series from hour 7.5 to hour 11 in Fig. 1(a). The harmonic signals are clear even at distant stations BCC and TEH.

Note that the line was not 'marked' by the authors. It is the result of spectral analysis and the extent of this line (about 4 hr) exactly matches the duration of this experiment.

During the experiments, amplitudes at the source were maintained at a fairly constant level. Fig. 2(b) shows the integrated spectral amplitudes between 1.62 and 1.66 Hz from the hour 6 to the hour 14. While there exists an overshooting peak at the beginning of this experiment, the amplitudes in all three components remain almost constant during this 4 hr experiment.

Figs 3(a) and (b) show the waveforms in the time domain and their three-component Fourier amplitudes at four selected locations. Stations (locations shown in Fig. 1) and their distances from the

Millikan library are, respectively, PAS at the distance of 4.36 km, MWC at 11.47 km, BCC at 101.43 km and TEH at 130.88 km. Fig. 3(a) only shows the time-domain waveforms for the north–south components (BHN), but the basic characteristics are the same for other components; namely, at close distances, the time-domain waveforms have box-car like envelopes (PAS and MWC). But such box-car like envelopes disappear at far away stations (BCC and TEH). In the frequency domain, however, harmonic signals are clear even at these teleseismic stations, as evidenced by spectral amplitude peaks between about 1.637 and 1.638 Hz.

This frequency range (1.637–1.638 Hz) will be used for phase analysis later. While we casually refer to the north-south resonant frequency as 1.64 Hz, the real spectral peak is found between 1.637 and 1.638 Hz. Some nearby stations (such as PAS) show broader spectral width than this range but at teleseismic distances, only the frequency range between 1.637 and 1.638 Hz shows significant signals.

3.2 Characteristics in amplitude data

The results in this section are all from the experiment on 2001 August 3 (the north–south shaking experiment). The basic characteristics were the same with the experiment on 2002 September 23. Using the 4-hr long records, we measured Fourier spectral amplitudes for 70 stations. Our stacking approach for spectral analyses is described in the Appendix. Measured spectral amplitudes are plotted on a map in Fig. 4 for the vertical component (Z). In this figure, a larger area in Southern California is shown at top and the Los Angeles basin area is shown below.

The white circle indicates the location of the Millikan library. Amplitudes are represented by diameters of circles, which are in the logarithmic scale as indicated on the right-hand side of Fig. 4.

The bottom panel indicates, at least for this small region, that amplitudes do not necessarily decrease with distance. This is because shallow crustal layers have strong amplification effects such as those found in the Los Angeles basin that is just to the south side of the Millikan library. Both the radial (R) and the transverse component (T) maps also show similar patterns.

If all data were examined on a larger scale, there emerges a systematic trend with distance; Fig. 5 shows the combined data from vertical, radial and transverse components. This is a log–log plot and demonstrates existence of a systematic, decreasing trend with distance. The dash line is shown as reference and has the gradient of (−5/3). This gradient was not determined by fitting data but it is shown here simply as a reference. Note that, for these data points, we have not made any corrections for geometrical spreading or attenuation.

In addition to a generally decreasing trend, there are two important features in this plot. One is the size of vertical scatter. This vertical scatter changes with distance but in general the amplitudes scatter about two-orders of magnitude variations (factor of 100) for distance less than 50 km and about an order of magnitude variation (factor 10) beyond 50 km. These scatters are related to local amplification effects under each station. The other is a change in the trend (gradient) at distance about 50 km. The amplitude decreasing trend has a different gradient for less than 50 km in comparison to that for beyond 50 km. This sharp change about 50 km will become even clearer in the semi-log plots that we analyse later (Figs 11 and 12).

Azimuthal variations in amplitudes are shown in Fig. 6, separately for distances less than 50 km and beyond 50 km. In general, we do not see any specific indications for the radiation patterns at the source (Millikan) that are consistent with the north–south force. However, the fact that they are not quite random with azimuth indicates that these waves are not quite stochastic random waves at 1.64 Hz.

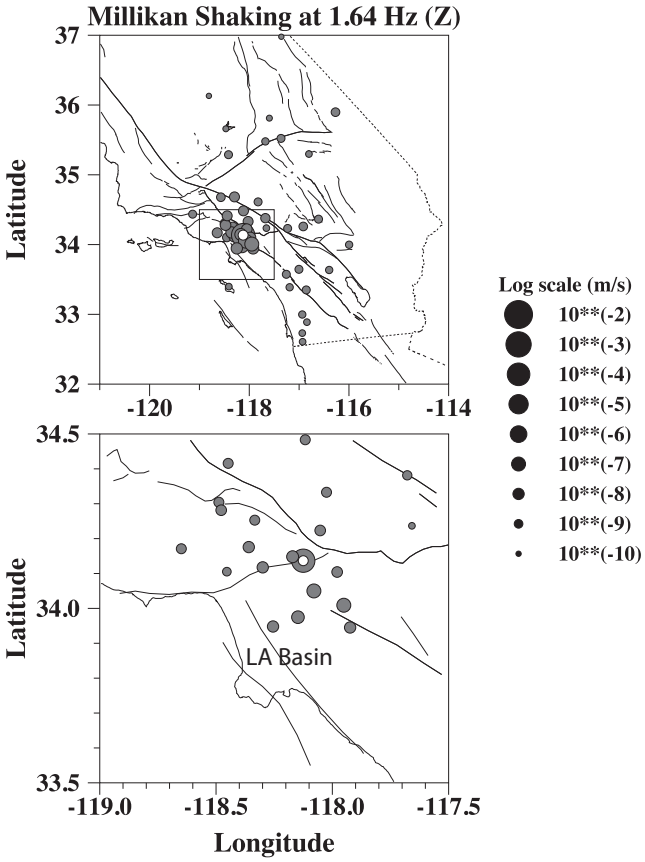

Figure 4. Measured spectral amplitudes (vertical component Z) for 70 stations. Amplitudes are expressed by radius (note the log scale). The white circle in each panel is the location of the Millikan library. The bottom panel is an enlarged plot for the boxed area (LA Basin) in the top panel.

4 NATURE OF SIGNAL

Since our data are very narrow-band harmonic signals that are quite different from regular seismograms, a natural question is what are these signals made of? Are they mainly body waves or surface waves? In order to answer this question, we performed theoretical analysis based on numerical elastic-wave simulations.

Fig. 7 shows an area (red rectangle) in which we performed the finite-difference simulation of seismic waves. The white triangle at latitude about 34° (SRC) is the location of the Millikan library. The white triangle to the north (RECV) is the location of a seismic station, at about an epicentral distance of 150 km. The results in Figs 8–10 are for this pair of stations.

We used a staggered-grid finite-difference method for simulations of seismic waves for this region. For a seismic structure, we adopted a regional 3-D seismic velocity model developed by the Southern California Earthquake Center (SCEC). Specifically, we used the model called SCEC CVM-H 11.9.0 (http://scec.usc.edu/scecpedia/CVM-H_User_Guide).

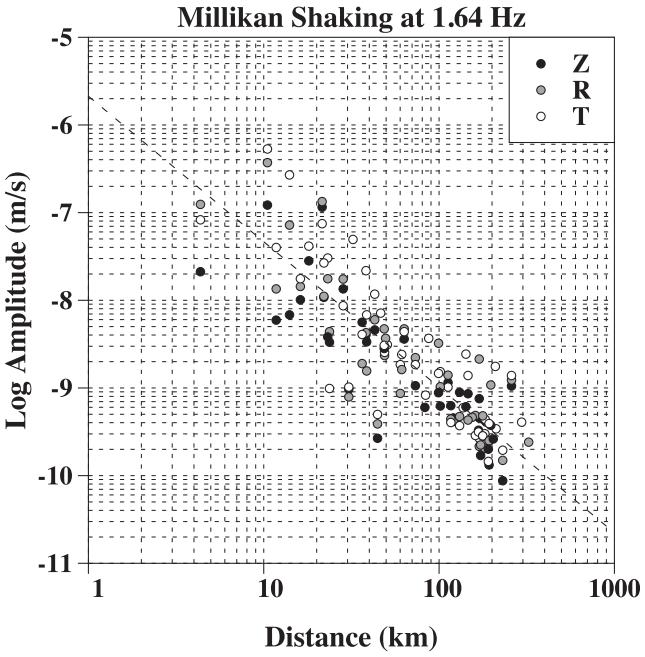

Figure 5. A log–log plot of all spectral amplitude data (all three components). Dash line is only a reference and has the gradient (−5/3).

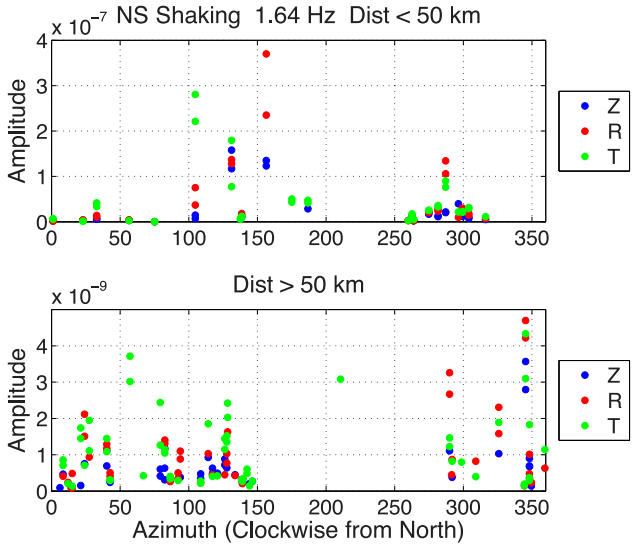

Figure 6. Plot of spectral amplitude as a function of azimuth. In general, there is no hint of radiation pattern, although the amplitudes are not quite random either (as a function of azimuth) (top) all data at distances below 50 km are plotted. (bottom) All data beyond 50 km.

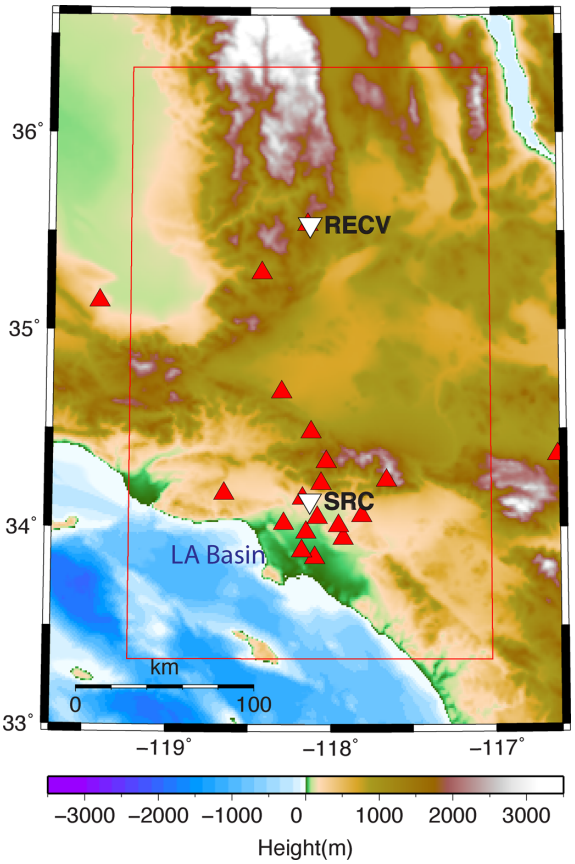

Figure 7. The area for finite-difference simulation. The white triangle to the south is the Millikan library (SRC). The white triangle to the north (RECV) is the location of station in Figs 8–10. A large green area (LA Basin) shows an approximate boundary of the Los Angeles basin.

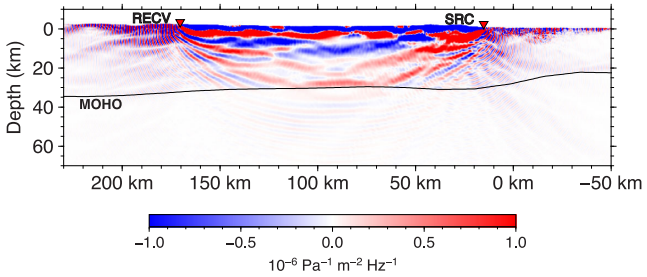

Figure 8. The rigidity kernel computed for the source at SRC (Millikan) and the receiver at RECV. Amplitudes in the kernel K_μ are normalized and plotted in red and blue. There is a turning *S* wave (bottoming about 30 km) but near-surface amplitudes (surface waves) are much higher. The wavefield is dominated by *SH*-type waves in this case.

We used a Japanese supercomputer TSUBAME at Tokyo Institute of Technology for these computations. This is one of the fastest GPU computer in Japan and the finite-difference simulation code, which can incorporate the effects of topography, oceanic layer and structural heterogeneity, has been developed to take advantage of its GPU architecture (Okamoto *et al.* 2010, 2012, 2013). In addition to elasticity from SCEC CVM-H, we incorporated the effects of attenuation. For attenuation parameters, we assigned Q_P and Q_S based on seismic velocities and the range was 170–850 for Q_P and 100–500 for Q_S which is a common practice for numerical simulations (e.g., Bielak *et al.* 2010). The τ method (Blanch *et al.* 1995) with a slight modification was used for attenuation. Parameters for the simulations are given in Table A1.

The key to identify the nature of waves is in the adjoint kernels. These kernels are now often used for waveform inversion of seismic data for earth structure (Tarantola 1984; Tanimoto 1990; Tromp *et al.* 2005; Zhao *et al.* 2005). Here we use the property that shape of kernels provide physical insights into the kinds of seismic waves. For computations, we used the following formulas.

$$\delta u = \int \{K_\rho(\mathbf{r})\delta\rho + K_\lambda(\mathbf{r})\delta\lambda + K_\mu(\mathbf{r})\delta\mu\}\mathrm{d}\mathbf{v} \qquad (1)$$

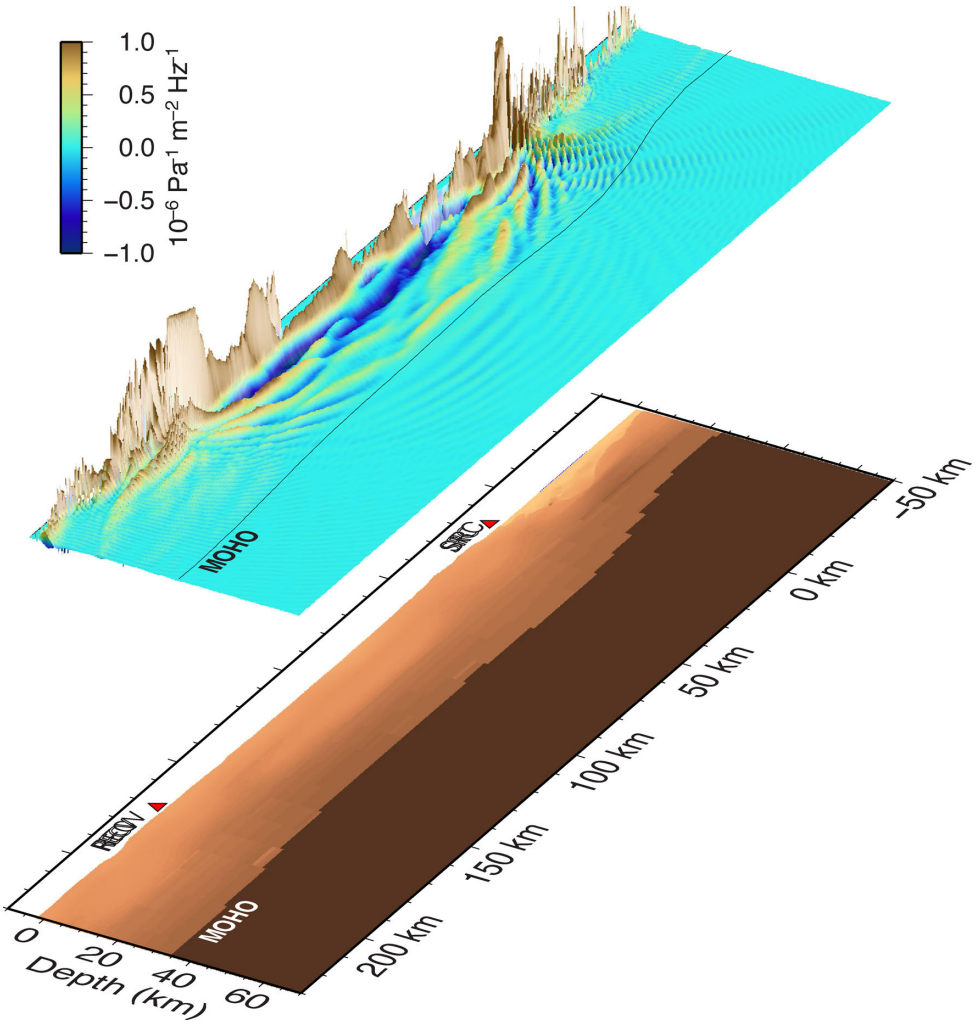

Figure 9. (top) Same kernel with Fig. 8 but plotted in a 3-D plot. Predominance of near-surface amplitudes is obvious. (bottom) *P*-wave structure of SCEC CVM-H 11.9.0. MOHO shows the highest contrast between dark brown and light brown.

with

$$K_\rho = \omega^2(u_x^A u_x + u_u^A u_y + u_z^A u_z),$$
$$K_\lambda = -\Delta^A \Delta,$$
$$K_\mu = -2\mathrm{e}_{ij}^A \mathrm{e}_{ij}. \qquad (2)$$

In (1) and (2), δu means a perturbation in displacement (of a chosen direction) caused by perturbations in structure for density ($\delta\rho$) and two elastic constants ($\delta\lambda$ and $\delta\mu$). The three kernels were derived from angular frequency (ω), displacements (u_x, u_y, u_z), the volumetric strain (Δ) and the shear strain (e_{ij}) in the simulated wavefields.

Following Tarantola (1984), we compute two wavefields; the forward wavefield with the source at the Millikan library and the adjoint wavefield with the source at the receiving seismic station. At Millikan, the source is a sinusoidal horizontal force at the surface. For the adjoint wavefield, we put a single force at the surface in the direction of a seismic component and simulated the wavefield. In the above formulas, the quantities with the superscript A are those in the adjoint wavefield.

Fig. 8 shows a depth-slice of the rigidity kernel, K_μ. The Millikan library is indicated by SRC and the receiver is indicated by RECV. This depth slice is along the north–south direction. Amplitudes of the rigidity kernel are plotted by blue and red where the scale is given below.

The source is a sinusoidal source in the east–west direction for this result (thus at 1.12 Hz). The force is acting in-and-out of plane in this figure. The receiver component in Fig. 8 is also the east–west direction. The rigidity kernel dominates in this case because most of the waves are *SH* (related) waves.

Fig. 8 shows a feature related to a turning *S* (*SH* body) wave near the Moho (depth about 30 km) as well as strong Love waves with large near-surface amplitudes. The dominance of near-surface amplitude can be identified easier in the 3-D plot in Fig. 9 where the near-surface amplitudes are clearly much larger than deep turning body waves. In the bottom panel, *P*-wave velocity model of SCEC CVM-H is shown as reference.

The normalized density kernel, K_ρ, and the λ kernel, K_λ, are shown in Fig. 10. The density kernel (top) is most likely related to *SH* waves (Love waves) but the λ kernel cannot be related to *SH*-type waves. A most likely reason for existence of non-zero K_λ is because of the conversion from Love waves to Rayleigh waves near the source due to a 3-D structure of the regional reference model (SCEC CVM-H). Conversion must be close to the source as we can trace its surface amplitudes all the way from the source to the receiver.

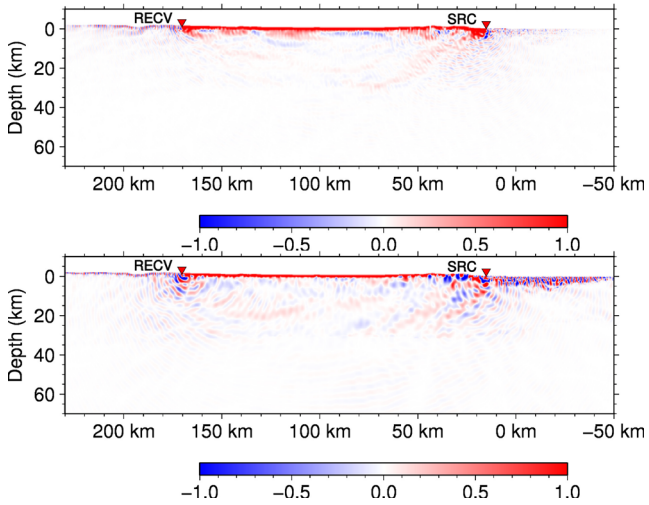

Figure 10. (top) Density kernel K_ρ. (bottom) The λ kernel K_λ. The λ kernel cannot be related to *SH*-type waves but exists because of conversion to Rayleigh waves. Since the medium is 3-D, the wavefield is mixed with *P–SV* type signals and *SH*-type signals.

We have performed these calculations for many other pairs of stations. In all cases, the main characteristics was the dominance of surface waves in the kernels. Both Rayleigh waves and Love waves exist in general and these surface waves had much larger amplitudes than body waves.

5 AMPLITUDE ANALYSIS

5.1 The parameter *QU*

Since the dominance of surface waves is clear, we adopted the assumption that the amplitude data may be interpreted as surface wave signals. This means, in terms of the amplitude-distance relation, we assume a relation

$$u(x) \propto \frac{B}{\sqrt{x}} \exp\left(-\frac{\omega x}{2QU}\right), \tag{3}$$

where x is the source–receiver epicentral distance, B is a coefficient, Q is attenuation parameter for a surface wave and U is its group velocity. The coefficient $1/\sqrt{x}$ arises from the far-field expression of the Bessel function (or a Legendre polynomial for a spherical case) and the exponential term is due to attenuation.

The data for the north–south shaking experiments are shown in Fig. 11 where we plotted the vertical, the radial and the transverse amplitudes. As we cannot see clear differences in trends among three components, we used all data in the analysis. The results from two experiments, one on 2001 August 3 and the other on 2002 September 23, were included in this data set.

Because we cannot see systematic differences among three components, it naturally leads to the conclusion that we are not distinguishing Rayleigh waves and Love waves. Because surface waves in a 3-D medium are mixed in general and conversion from one type to another may also occur, it is naturally difficult to distinguish. We still believe that Rayleigh and Love waves still maintain their characteristics for frequencies at 1.12 and 1.64 Hz, but amplitude information alone does not seem to be sufficient to distinguish them. Phase analysis in the next section seems to provide a different picture because vertical-to-vertical cross correlations often give different velocity from horizontal-to-horizontal cross correlations.

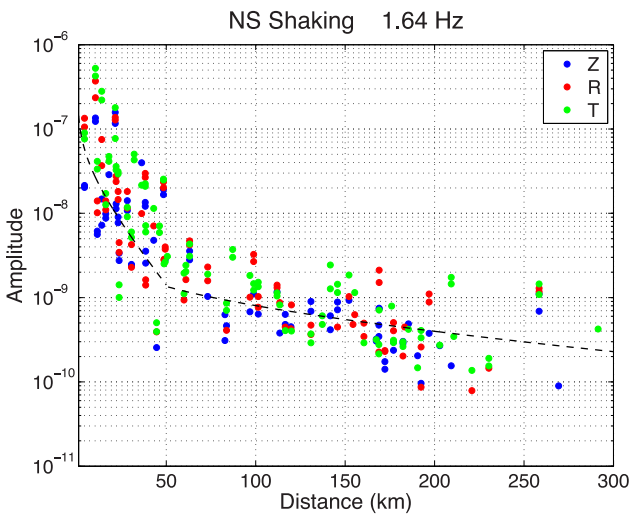

Figure 11. A semi-log plot of amplitude–distance data. The results from two experiments at 1.64 Hz (2001 August 3 and 2002 September 23) are combined. Fit for *QU* are shown (dash lines), separately for distance less than 50 km and beyond 50 km. Unit for amplitude is metres per second (unit for velocity) as we normalize the Fourier spectra by the length of time-series.

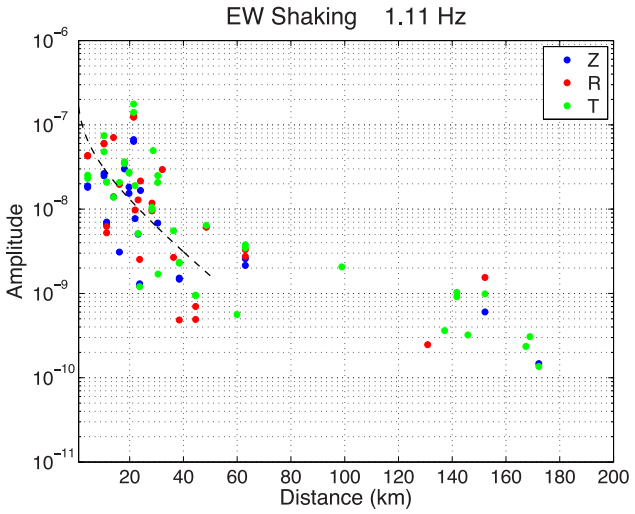

Figure 12. A semi-log plot of 1.11 Hz from two experiments (2002 February 19 and 2002 September 19). There are good data up to 180 km but a majority is confined to less than 50 km. Unit for amplitude is metres per second.

The dash lines were obtained from the fit to data by eq. (3). In this fitting procedure, we took the logarithm of both sides of (3) and applied a linear least-squares. There are in essence two independent parameters in this formula; one is B and the other is QU. The attenuation parameter Q and the group velocity U are not separable from this data set. Because there is a sharp change in gradient at about 50 km, the data were separately fit for distance less than 50 km and for distance beyond 50 km. The results for QU are $QU = 95 \pm 11$ for distance less than 50 km and $QU = 1454 \pm 224$ for distance beyond 50 km. In both cases, the unit for Q is non-dimensional but the unit for U is km s^{-1}.

In a similar manner, the results for the east–west shaking experiments conducted on 2002 February 18 and 2002 September 19, are shown in Fig. 12. For these lower frequency experiments (1.12 Hz), the number of stations with good signals is much less and especially fewer beyond 50 km. The result for the data for distance less than

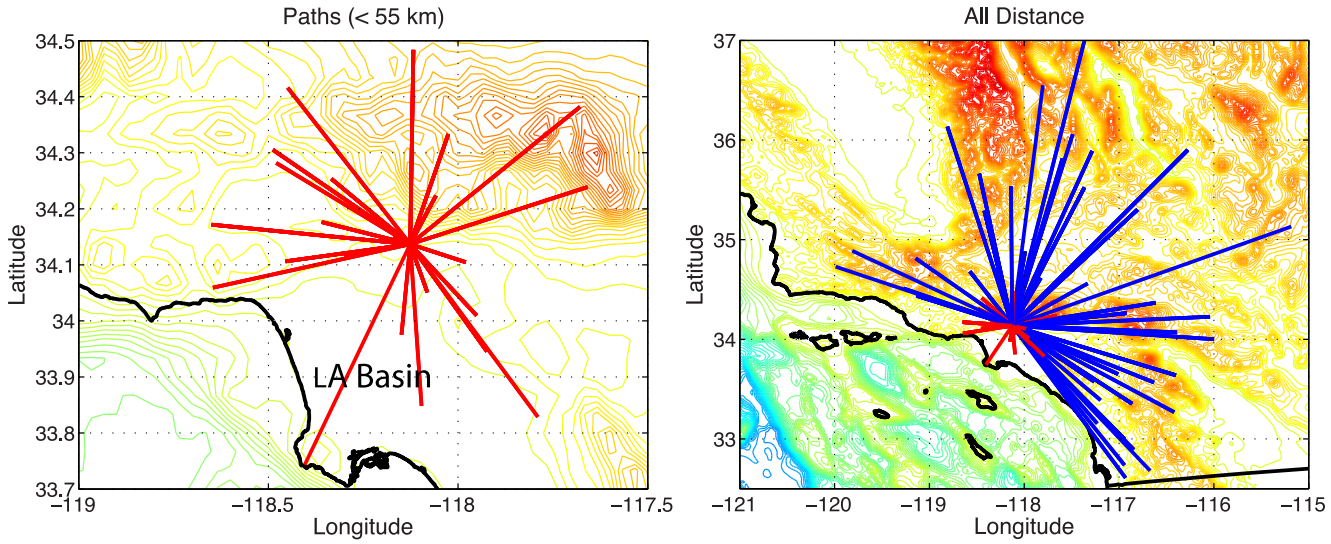

Figure 13. (Left-hand side) Paths in short-distance data (less than 50 km) for the two 1.64 Hz experiments (Fig. 11). (Right-hand side) Blue paths are for long-distance data (beyond 50 km). In order to see the comparison better, the same short-distance data (red) are plotted.

50 km is $QU = 76 \pm 16$ with the curve shown by a dash line in Fig. 12.

5.2 Cause of an abrupt change in amplitude–distance plot

Why is there an abrupt change in the gradients in amplitude-distance data at about 50 km? The exact cause of this feature is hard to delineate because of the limited amount of data but it seems to be related to the differences in the areas that were sampled by short-distance paths (less than 50 km) and the long-distance paths (beyond 50 km).

The two panels in Fig. 13 show the paths of data in Fig. 11. We simply used great-circle paths for this plot. There are clear differences in paths between the short-distance and long-distance data sets. The most important difference is the lack of paths in the Los Angeles basin in the long-distance data (blue in the right panel). The short-distance paths contain many paths in the Los Angeles basin. There is thus a clear hint that this abrupt change is related to the differences in structure between the basin (LA basin) and the surrounding regions. However, not all short-distance paths are in the Los Angeles basin. Some are in the hard-rock sites toward north. Therefore, we only claim that there is only a hint to this connection.

5.3 Large QU for long-distance data

The value for QU that we obtained for data beyond 50 km, $QU = 1454 \pm 224$, is quite large. A typical value for surface wave group velocity is 3–4 km s^{-1} but for higher frequency waves it may be 1–2 km s^{-1} at most. Then it implies that the Q values may be 750–1500. The Q values above 1000 may be a little hard to believe for high-frequency surface waves, especially when we have not removed the effects of scattering. Therefore, we suspect that our assumption of signals being surface waves may be violated for these long-distance data. We suspect that they could be special (body or surface) waves that propagated in efficient waveguides. We do not believe that the current SCEC CVM-H models have features to produce such waves.

6 PHASE ANALYSIS

6.1 Behaviour of phase

There is a station MIK in the Millikan library since May, 2001. By calculating cross correlations between MIK and a station in the network, we can in essence deconvolve the source–time function and derive spectral information that is relevant only to propagation in the medium. If the JWKB approximation is acceptable, the phase should be given by

$$\phi = \int_{\text{path}} k \, \mathrm{d}s - M\frac{\pi}{2} + \frac{\pi}{4}, \tag{4}$$

where the integration over the wavenumber k (of a surface wave) is along a propagation path from the Millikan library to a seismic station and M is the Maslov index that keeps track of the number of caustics along the path.

In order to see how phase varies in data, we used an approach with multiple, overlapping (time-domain) windows. Fig. 14 shows an example for the north-south shaking experiment on 2001 August 3 (Fig. 1a). The duration of experiment was 4 hr. Within this time interval, we took 75 windows with 1 hr length (W in Fig. 14) with each window shifted by 2 min. In order to avoid the effects from the initial overshoots in amplitudes (Fig. 2b), we started the time window from 7:30. Fig. 14 shows phase from cross correlations between 1.630 Hz and 1.645 Hz; phase from 75 windows are plotted in this figure. For this analysis, we use cross correlation between vertical components (Z–Z). In Section 6.3, we show the consistency of the results with the N–Z cross correlations where we cross-correlated the north–south component at MIK and the vertical component of a regional seismic station.

The main characteristics in Fig. 14 is the emergence of stable phase at about -50° (phase) for frequencies about 1.637 Hz. The peak of energy from harmonic oscillations is about this frequency. Outside the narrow frequency range of resonant oscillations, phase scatters because each time window contains different noise that causes phase to scatter widely. But within the frequency range of resonant frequency, phase becomes almost constant. This means that phase (difference) between MIK and station PAS is locked and moves coherently in time.

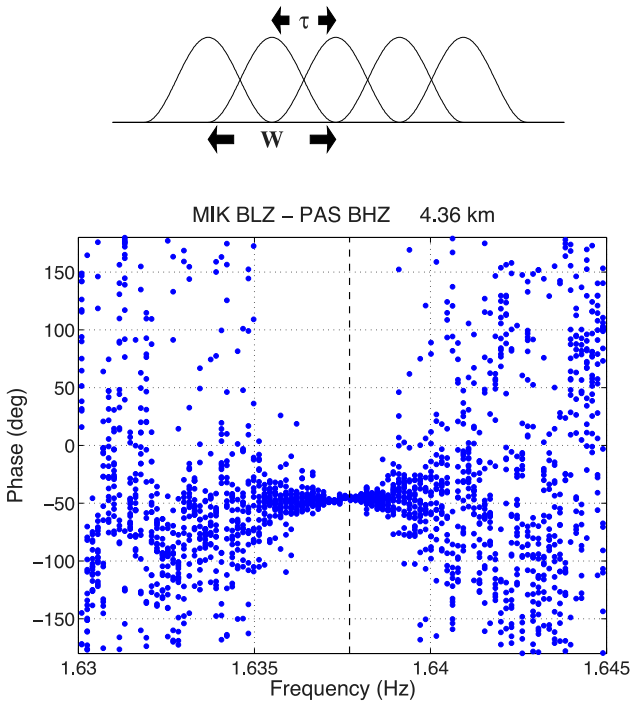

Figure 14. Phase from 1-hr long time window. Inside the range of the harmonic signals (near 1.637–1.638 Hz) phase is quite stable. Outside this range, phase scatters because noise can dominate the signals and vary from one window to another. Phase is stable for a range wider than 1.637–1.638 Hz for this station because of the short distance (4.36 km). For most other stations at farther distance, phase locking is confined to 1.637–1.638 Hz which coincides with the spectral peak in Fig. 3(b).

This observation suggests that, if we can resolve the number of phase cycles between the two stations, we should be able to retrieve phase velocity between the two stations. However, an unambiguous resolution of phase cycle is not possible because of short-wavelength nature of high-frequency waves. For example, at PAS, which is only 4.36 km away, there should be about 10 cycles as our later analysis on group velocity suggests. But it is not possible to determine it uniquely and distinguish it from 9 or 11 without additional information. For longer distance stations, this phase-cycle problem becomes even more severe as there can be more than a hundred cycles.

6.2 Group velocity from phase derivative

Because of the ambiguity in phase cycles, we turned to group velocity measurements from phase derivatives. Note that if we differentiate (4) by frequency f, we obtain

$$\frac{\partial \phi}{\partial f} = 2\pi \int_{\text{path}} \frac{\mathrm{d}s}{v_g} = \frac{2\pi X}{\overline{v}_g}, \tag{5}$$

where v_g is group velocity, $\overline{v}_g$ is the average group velocity along the path and X is the path length. The quantity we obtain will be $\overline{v}_g$ by measuring $\partial\phi/\partial f$ from data.

We use the great-circle distance for X in the following analysis. This is not quite correct as high-frequency waves do not propagate along great-circle paths, but deviations from correct group velocities may not be so large. We believe the results should be good approximations.

The key step in the group-velocity analysis will be the determination of $\partial\phi/\partial f$ from phase data. Two examples are shown in Figs 15(a) and (b). Phase data, similar to Fig. 14, are shown. For this measurement, we explored a different parameter range for W and τ and adopted to use $W = 40$ min and $\tau = 1$ min. Within the 4-hr time window, we had 180 time windows.

In order to determine phase derivative with respect to frequency, we stacked all 180 spectra and derived phase for this stacked spectra. This is shown by blue line in each figure. In Figs 15(a) and (b), both the top panel and the bottom panel show the same blue curve (phase), retrieved this way. Then we fitted a linear line for phase data between 1.637 and 1.638 Hz where significant oscillation energy exist (and phase is stable).

Fig. 15(a) shows the case for the station pair MIK–PAS for which the epicentral distance is 4.36 km, azimuth of PAS at MIK is 287.12° (clockwise from north) and the obtained group velocity was 0.267 ± 0.039 (km s^{-1}). These information are given at top of each figure (Figs 15a and b). The results for MIK–JVA are shown in Fig. 15(b) (group velocity 1.832 ± 0.161 km s^{-1}). Fig. 15(b) shows an example that this stacking worked quite well, as phase scatter seems quite large but the stacked phase clearly show a linear trend within the frequency band 1.637–1.638 Hz.

This is also one of the reasons that we should limit the frequency range of this analysis to 1.637–1.638 Hz. The linearity of phase is only clear for this frequency range. If we extended this range any further, say 1.636–1.639 Hz, we would not get a correct estimate because the linear trend does not exist outside 1.637–1.638 Hz.

6.3 Comparison between *ZZ* and *NZ* correlations

Phase analysis in the previous section was performed for vertical components. Here we refer to it as *ZZ* cross correlation. In order to check the stability of our measurements, we also examined the north–south component of data at MIK for the cross-correlations. For a network station, we still used a vertical component. We refer to this as *NZ* cross correlation. Fig. 16 shows the case for station CHF, where the top panel shows the *ZZ* cross correlations and the bottom panel shows *NZ* cross correlations (between the NS component at MIK and the *Z* component at CHF). Behaviour of stacked phase below the frequency 1.637 Hz and behaviour for above the frequency 1.638 Hz show that phase differs much between *ZZ* cross correlation and *NZ* cross correlations. However, the gradient of phase between 1.637 and 1.638 Hz became almost identical and both cases led to group velocity estimate of 1.319 ± 0.168 (km s^{-1}).

We also tried cross correlations among different components, including those among horizontal components. We found some consistent values but also inconsistent (different group velocity) values. We believe the consistency between *ZZ* and *NZ* arose from the fact that most results are for Rayleigh waves; different values probably arose because of Love waves. However, we have not been able to verify them independently and are thus publishing only *ZZ* (and *NZ*) cross-correlation results.

6.4 Group velocity results

Using the above approach, we estimated group velocity for 25 stations. There were 70 stations for amplitude data but phase measurements for other stations were not as successful as that in Fig. 16, mostly because phase scatter was much larger and phase gradient was not reliably measured. But for those 25 stations, the consistency was confirmed between *ZZ* and *NZ* cross correlations.

Fig. 17(a) shows group velocity results, plotted as a function of distance. The distance is the epicentral distance from the Millikan

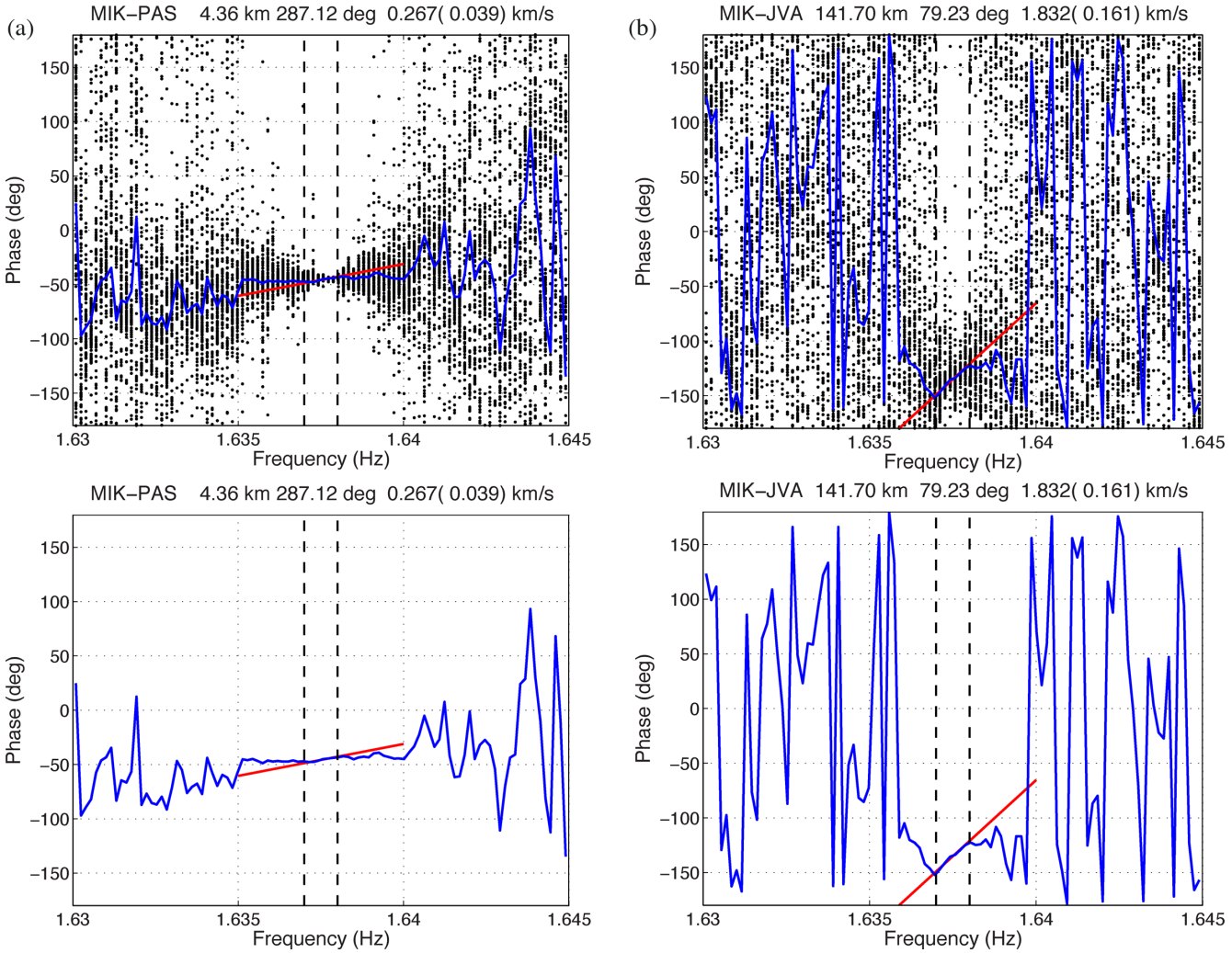

Figure 15. (a) Two dash lines indicate 1.637 and 1.638 Hz. The gradient was obtained from stacked phase from which we estimate group velocity. This is for the pair MIK and PAS at epicentral distance 4.36 km. The azimuth of PAS at MIK is 287.12° (clockwise from north). Group velocity was 0.267 ± 0.039 km s^{-1}. (b) Same with Fig. 15(a) except that this is for a pair MIK and JVA at distance 141.70 km. Group velocity was 1.832 ± 0.161 km s^{-1}. Note the linearity between 1.637 and 1.638 Hz which deviates outside.

library. Under those conditions, the estimates are shown by solid circles and their uncertainties are plotted by vertical bars.

For stations with distance less than 50 km, group velocities are typically 0.5 km s^{-1} or less with an exception (CHF). In fact, group velocity is mostly lower than 1 km s^{-1} up to distance about 120 km (BBR). For stations beyond 120 km, group velocity is slightly higher, between 1 and 2 km s^{-1}, but seems to be bounded on the upper side by 2 km s^{-1} with the exception of TEH. Systematically higher velocities beyond 120 km (TEH and stations to the right in Fig. 17a) may also suggest that they are not surface waves as we discussed in Section 5.3.

Fig. 17(b) shows the same results for 25 stations but the results are plotted against azimuth (station azimuth measured at the Millikan library). An important characteristics of this figure is the lack of measurements in the azimuth range of the Los Angeles basin except for RUS and LGB. An approximate range of azimuth for the Los Angeles basin is indicated in the figure by an arrow. While amplitudes were large for these stations in the Los Angeles basin, and thus were included in Fig. 11 (and Fig. 13), but their phase scatter was quite large. This precluded us to measure group velocity in the Los Angeles basin except for RUS and LGB. Nonetheless, derived group velocities to LGB and RUS are much lower than 500 m s^{-1}, suggesting very low group velocities in the basin.

Fig. 18 shows the same results on a map with colour, indicating the range of group velocity. Red means group velocity less than 1 km s^{-1}, green means between 1 and 2 km s^{-1} and blue above 2 km s^{-1} (TEH). Lack of paths to the azimuth of Los Angeles basin is also obvious in this figure. There does not seem to be particular systematics in these results, although it may be due to coarse path coverage that we can get for the moment.

7 CONCLUSION

Seismic wavefields generated by resonant-shaking experiments of the Millikan Library, on the campus of California Institute Technology (Pasadena, California, USA), were analysed. Because the resonant-shaking frequencies are 1.12 Hz (the east–west direction) and 1.64 Hz (the north–south direction), the wavefields provided opportunities for studying high-frequency seismic wave propagation in Southern California. Our results demonstrate that an active-source

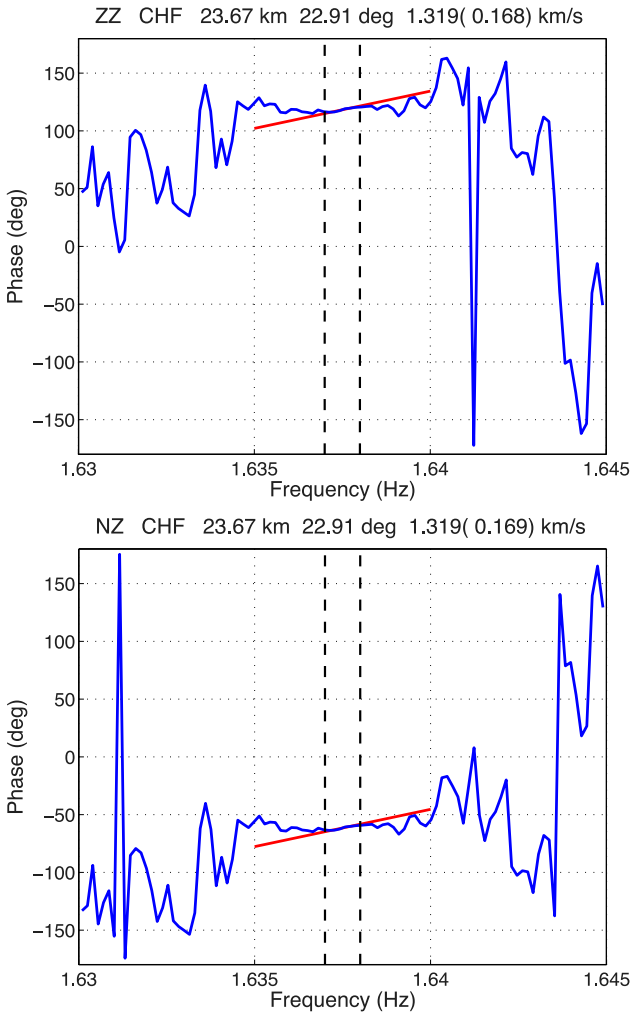

Figure 16. Most of cross-correlations are done for vertical to vertical seismograms. In order to check it, a north-south component (MIK) to vertical correlation (CHF) was taken Top is ZZ cross-correlation and bottom is NZ correlation. While phase is different between top and bottom outside the main frequency band (dash lines), the gradient within the main frequency band remains the same. Group velocity is basically the same from ZZ and NZ cross-correlations.

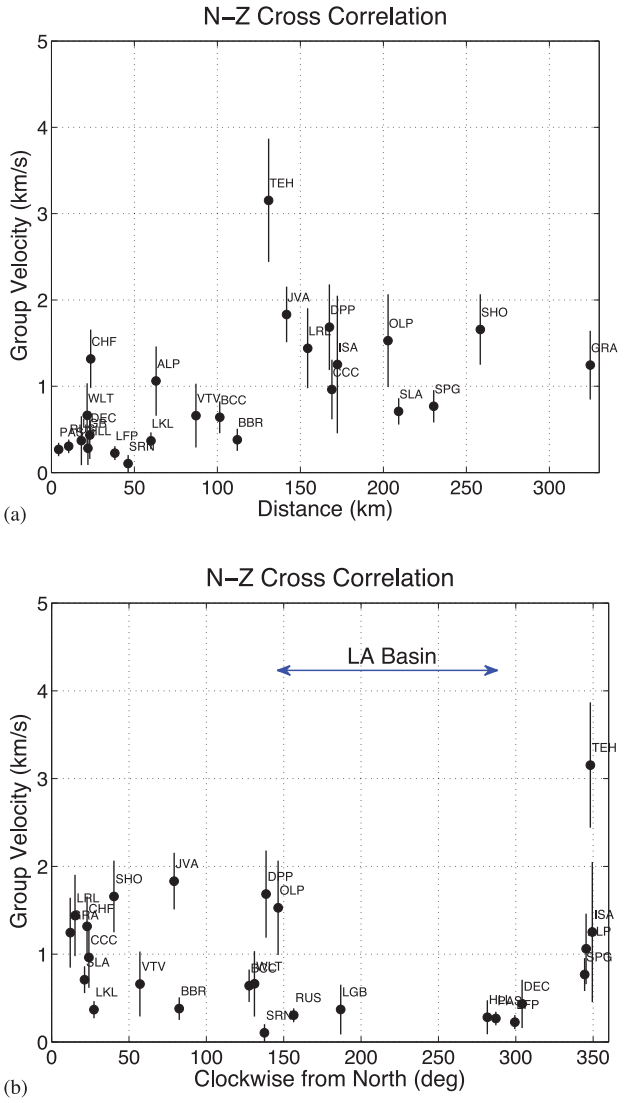

Figure 17. (a) Group velocity versus distance plot for 25 stations. We consider them as Rayleigh wave group velocity as they are from *NZ* (and *ZZ*) cross-correlation. Except for TEH, all group velocities are below 2 km s^{-1}. For distances below 50 km, group velocity is mostly below 0.5 km s^{-1}. (b) Same results with Fig. 17(a) but group velocities are plotted with azimuth at MIK. The approximate range of azimuth for the Los Angeles basin is shown by arrow. LGB and RUS are the only exceptions.

experiment by resonant shaking of a building is a feasible approach for high-frequency seismic wave studies.

Two experiments at each frequency were analysed; for the north–south shaking experiments (1.64 Hz), the harmonic signals were observed up to distance 323 km in one experiment and up to 396 km in another experiment. For the east-west shaking (1.12 Hz), the maximum distance was close to 200 km but most good signals were confined to less than 50 km.

Numerical simulations indicated that the predominant signals were surface waves. Assuming that all signals were surface waves, we obtained estimates for the parameters QU, where Q is the attenuation parameter of surface waves and U is the group velocity of surface waves. There is, however, a major break in the amplitude–distance trend at a distance about 50 km; for data with distance less than 50 km, $QU = 95 \pm 16$, where U is in km s^{-1}. For data beyond 50 km, we obtained $QU = 1454 \pm 224$. For the 1.12 Hz experiments, there was also a change in trend at about 50 km but most good signals were only found for the distance range less than 50 km. We obtained $QU = 76 \pm 16$ for these short-distance data.

The fact that differences among three components are not clear, due to scatter, means we cannot tell whether those surface waves are dominated by either Rayleigh waves or Love waves.

This change in trend must be related to the regions sampled by waves, as the shorter distance data were dominated by paths in the Los Angeles basins while the longer distance data did not contain paths in the basin structures.

Through the cross-correlation between data at MIK (a station in the Millikan library) and data from the regional network, phase information was analysed. For many stations, we observed stable phase value for frequencies between 1.637 and 1.638 Hz, which meant that phase is locked between MIK and those network stations. While it was not possible to estimate phase velocity, because the number of cycles cannot be resolved for high-frequency waves, a stacking approach for multiple-window data allowed us to derive group velocity for 25 paths. Group velocity between MIK and

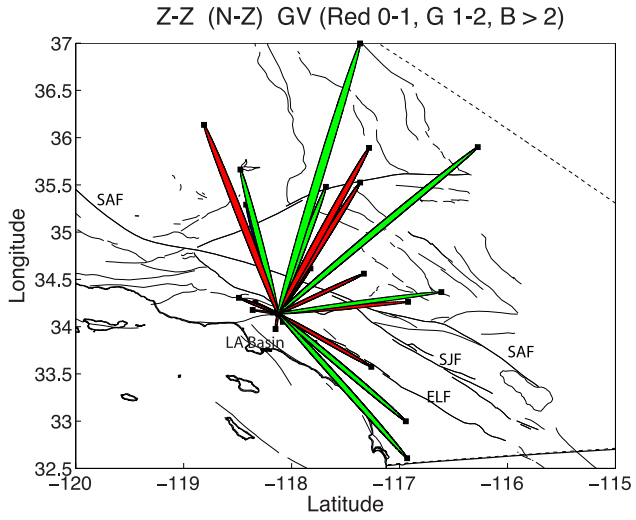

Figure 18. Same group velocity results are plotted on a map. Ted paths indicate group velocity less than 1 km s^{-1}, green between 1 and 2 km s^{-1} and blue faster than 2 km s^{-1} (there is only one). There does not seem to be any particular systematics in this plot.

network stations were mostly less than 2 km s^{-1}. For stations with distance less than 50 km, group velocity was mostly about 0.5 km s^{-1} with some variations. Combined with the estimate for *QU* from the amplitude–distance data, *Q* becomes 190 for distances less than 50 km. This estimate, however, contains uncertainties up to a factor of two as variations in group velocity estimates exist from station to station. Because of the agreement from *NZ* and *ZZ* cross correlations, we believe the results from phase analysis are relevant to Rayleigh waves.

ACKNOWLEDGEMENTS

This research was supported by the Southern California Earthquake Center. SCEC is funded by NSF Cooperative Agreement EAR-1033462 and USGS Cooperative Agreement G12AC20038. The SCEC contribution number for this paper is 1908. This work was also supported by 'Joint Usage/Research Center for Interdisciplinary Large-scale information infrastructure' in Japan (Project ID: 13-NA-29).

REFERENCES

Bielak, J.R. *et al.*, 2009. The ShakeOut earthquake scenario: verification of three simulation sets, *Geophys. J. Int.,* **180,** 375–404.

Blanch, J.O., Robertson, J. & Symmes, W., 1995. Modeling of a constant Q: methodology and algorithm for an efficient and optimally inexpensive viscoelastic technique, *Geophysics,* **60,** 176–184.

Bradford, S.C., Clinton, J.F., Favela, J. & Heaton, T.H., 2004. Results of Millikan Library forced vibration testing, *Earthquake Engineering Research Laboratory,* Report No. EERL 2004-03, California Institute of Technology.

Clinton, J., 2004. Modern digital seismology—instrumentation, and small amplitude studies for the engineering world, *PhD thesis,* California Institute of Technology.

Clinton, J., Bradford, S.C., Heaton, T.H. & Favela, J., 2006. The observed wander of the natural frequencies in a structure, *Bull. seism. Soc. Am.,* **96,** 237–257.

Favela, J., 2004. Energy radiation from a multi-story building, *PhD thesis,* California Institute of Technology.

Foutch, D.A., 1976. A study of the vibrational characteristics of two multi-story buildings, *PhD thesis,* California Institute of Technology.

Foutch, D. & Jennings, P., 1978. A Study of the apparent change in the foundation response of a nine-story reinforced concrete building, *Bull. seism. Soc. Am.,* **68,** 219–229.

Hauksson, E. & Shearer, P., 2006. Attenuation models (Qp and Qs) in three dimensions of the southern California crust: inferred fluid saturation at seismogenic depths, *J. geophys. Res.,* **111,** B05302, doi:10.1029/2005JB003947.

Jennings, P., 1970. Distant motions from a building vibration test, *Bull. seism. Soc. Am.,* **60,** 2037–2043.

Jennings, P. & Kuroiwa, J., 1968. Vibration and soil-structure interaction tests of a nine-story reinforced concrete building, *Bull. seism. Soc. Am.,* **58,** 891–916.

Kohler, M., Heaton, T. & Bradford, S.C., 2007. Propagating waves in the steel, moment-frame factor building recorded during earthquakes, *Bull. seism. Soc. Am.,* **97,** 1334–1345.

Kuroiwa, j. H., 1969. Vibration test of a multistory building, *PhD thesis,* California Institute of Technology.

Newton, C. & Snieder, R., 2012. Estimating intrinsic attenuation of a building using deconvolution interferometry and time reversal, *Bull. seism. Soc. Am.,* **102,** 2200–2208.

Okamoto, T., Takenaka, H., Nakamura, T. & Aoki, T., 2010. Accelerating large-scale simulation of seismic wave propagation by multi-GPUs and three-dimensional domain decomposition, *Earth Planets Space,* **62,** 939–942.

Okamoto, T., Takenaka, H., Nakamura, T. & Aoki, T., 2012. Large-scale simulation of seismic-wave propagation of the 2011 Tohoku-Oki M9 earthquake, in *Proceedings of the International Symposium on Engineering Lessons Learned from the 2011 Great East Japan Earthquake,* pp. 349–360.

Okamoto, T., Takenaka, H., Nakamura, T. & Aoki, T., 2013. Accelerating large-scale simulation of seismic wave propagation by multi-GPUs and three-dimensional domain decomposition, in *GPU Solutions to Multi-scale Problems in Science and Engineering,* Chapter 24, pp. 375–389, eds Yuen, D.A. *et al.*, Springer-Verlag.

Snieder, R. & Safak, E., 2006. Extracting the building response using seismic interferometry: theory and application to the Millikan Library in Pasadena, California, *Bull. seism. Soc. Am.,* **96,** 586–598.

Tanimoto, T., 1990. Modeling curved surface wave paths: membrane surface wave synthetics, *Geophys. J. Int.,* **102,** 89–100.

Tarantola, A., 1984. Inversion of seismic reflection data in the acoustic approximation, *Geophysics,* **49,** 1259–1266.

Tromp, J., Tape, C. & Liu, Q., 2005. Seismic tomography, adjoint methods, time reversal and banana-doughnut kernels, *Geophys. J. Int.,* **160,** 195–216.

Zhao, L., Jordan, T.H., Olsen, K.B. & Chen, P., 2005. Frechet Kernels for Imaging Regional Earth Structure Based on Three-Dimensional Reference Models, *Bull. seism. Soc. Am.,* **95**(6), 2066–2080.

APPENDIX A: DETAIL ON SPECTRAL ANALYSIS

In order to make our results reproducible, we give details on our spectral computations. In this study, instead of using a whole time interval of experiments, we used a stacking approach with overlapping windows. We did this because, if one were to compute spectra for a 4 hr length (as was the case for Fig. 3b, the only exception in this paper), the spectral peak contains quite complicated shape within a narrow frequency band. This is not bad if data were perfect for all stations but some stations contained glitches and gaps. In order to be able to remove such effects, we used shorter time windows and took the averages from glitch/gap free time portions. But it required some understanding of the effects from window length and time-shift.

Fig. A1 shows our general concept. The time-window length is W and the time-shift between adjacent windows is τ. Figs A2 and A3

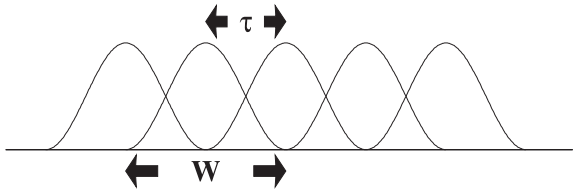

Figure A1. For spectral computations and cross-correlation computations, we used multiple time windows with length W and the shift τ.

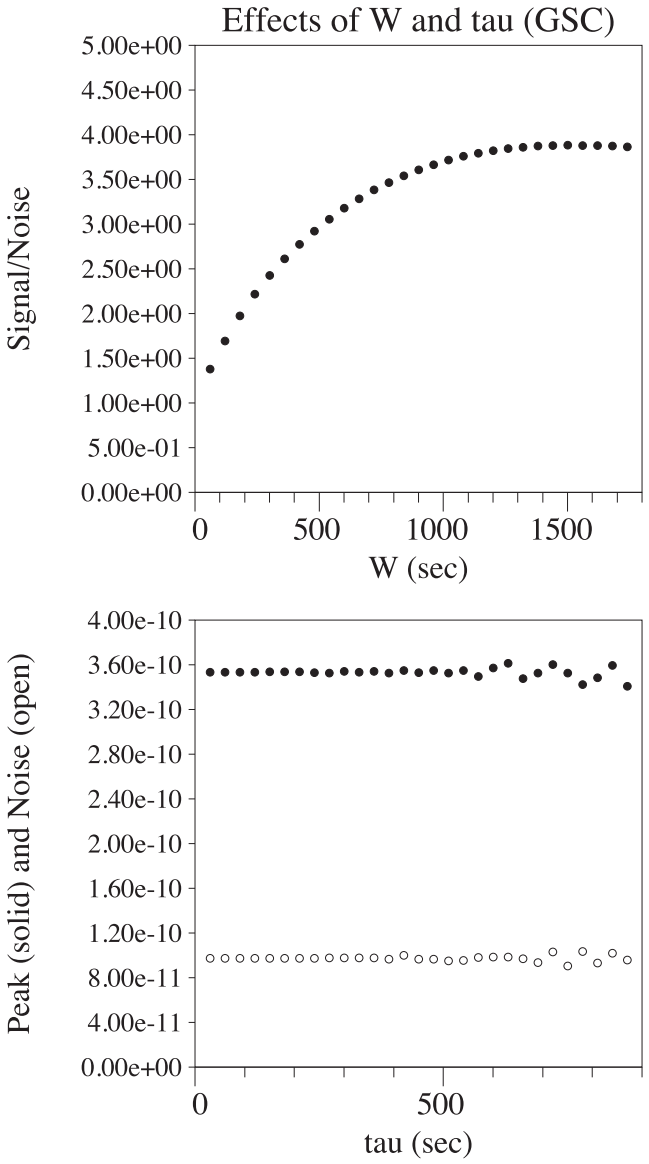

Figure A2. In order to find optimum time-shift and time-window length, we computed the signal-to-noise ratios with different choices. If the window is too short, we cannot get a good signal-to-noise ratio. This is for station GSC. After some numerical experiments, we chose $W = 1200$ s and $\tau = 200$ s for spectral amplitude computations.

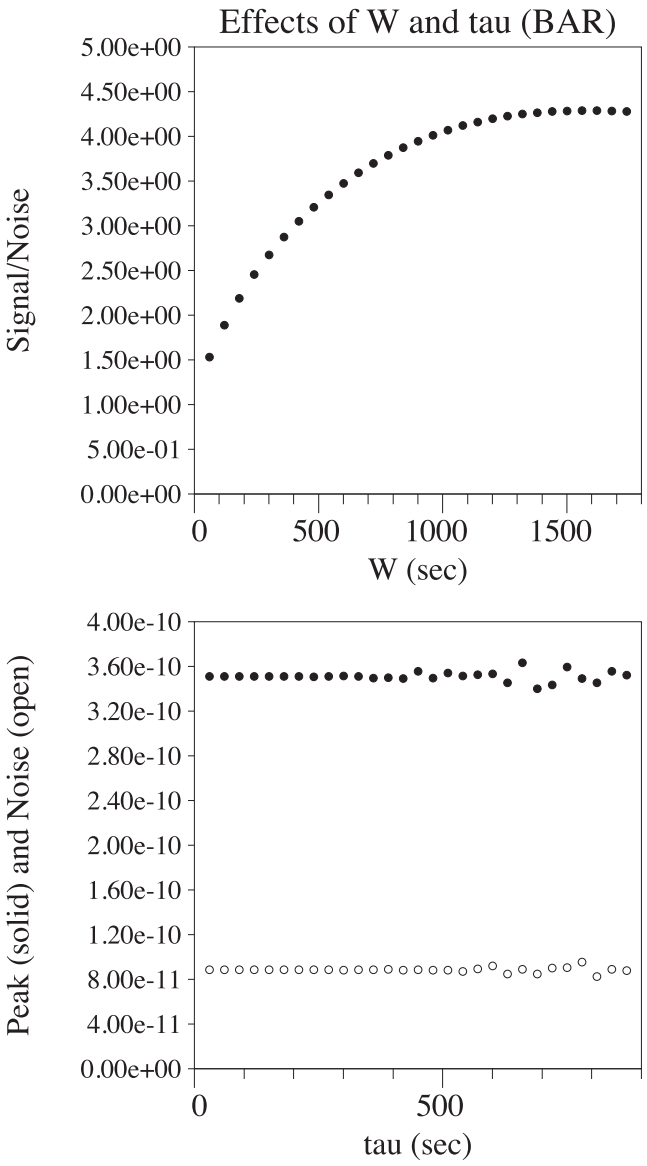

Figure A3. Same with Fig. A2 except that this is for a different station (BAR).

Table A1. Simulation parameters.

Grid size $NX \times NY \times NZ$ (X,Y: horizontal, Z: vertical)	4160 × 2560 × 1040
Time steps	30 000
Δx (uniform grid spacing)	0.08 km
Δt (time increment)	0.004 s
Approximate constant Q bandwidth	0.1–10 Hz
Number of used GPUs (= number of subdomains)	520
Total computation time	1.37×10^4 s

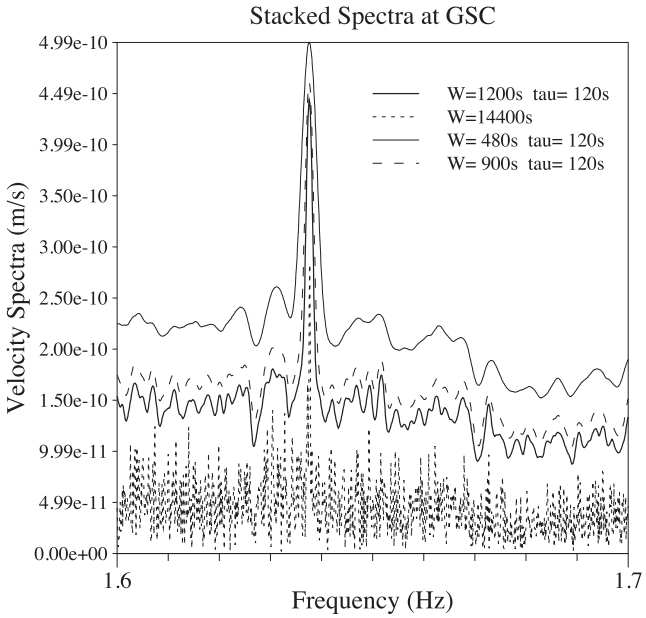

Figure A4. Effects of different choices of W and τ.

show the results of varying W and τ for the two stations GSC and BAR. In both cases, the signal-to-noise ratios suffer if the window length is less than about 1000 s. The effects from the time-shift τ are relatively constant but both the peak and the noise start to show some scatters above 500 s. We therefore adopted $W = 1200$ s and $\tau = 120$ s for our spectral computations.

Fig. A4 shows comparisons from four different cases of W and τ. Our final choice is given by the thick line ($W = 1200$, τ=120). The case with $W = 14\,400$ (4 hr) is just one window and involves no stacking. Obviously shorter the length of time-series, the widths of spectral peaks become broader. The spectral peak with $W = 14\,400$ s shows some complexity within the peak (Favela 2004) as well as some roughness in noise.

As there are pros and cons with these choices, this is just to clarify how we computed the spectral amplitudes, specifically those used for amplitude–distance plots.